#### **ORIGINAL ARTICLE**



# A multiphase simulation study of electrochemical discharge machining of glass

Ketaki Kolhekar 1 • Murali Sundaram 1 🗅

Received: 17 May 2019 / Accepted: 15 August 2019 © Springer-Verlag London Ltd., part of Springer Nature 2019

#### **Abstract**

Micromachining of glass has gained importance due to numerous applications of glass in microfluidics, optics, electronics, and biotechnology industry. Electrochemical discharge machining (ECDM) is an emerging nontraditional process which has the potential for micromachining of glass with minimal surface damages. Material removal during the machining of glass by ECDM involves thermal machining by electrical discharges between the tool and the gas film. The energy of these discharges is influenced by the gas film characteristics and affects the machining results. In this study, a combined approach of finite element simulation and experimentation is used to study the ECDM process to understand the impact of gas film characteristics on the overcut in machining. The multiphase simulation setup incorporates a combined electrochemical system of glass and electrolyte. The changes in the gas film characteristics due to the variations in the level of electrolyte and the corresponding changes in the overcut are studied. It was observed that the gas film thickness increased with an increase in the level of electrolyte and the gas film stability showed an opposite trend. This resulted in an increase in the overcut in the machining with the increase in the level of electrolyte. This trend observed in the simulation was validated with experimentation.

**Keywords** ECDM · Finite element simulation · Gas film · Glass · Micromachining · Overcut

#### 1 Introduction

Advanced materials such as engineering ceramics offer higher stiffness, higher strength, as well as better chemical resistance and electrical resistance compared to metals [1]. Glass exhibits additional advantages like better optical visuality and biocompatibility. A plethora of microscale applications using glass is emerging in several fields such as microfluidics and drug delivery [2]. Effective micromachining of glass is critical for the microscale applications of glass. Glass being a hard and brittle material, machining of glass by traditional methods faces considerable machinability challenges such as excessive tool wear and surface damages in the glass. Existing nontraditional micromachining technologies suitable for glass machining like abrasive machining, ultrasonic machining, chemical etching, and laser machining have several limitations such as surface

Electrochemical discharge machining (ECDM) has the potential to overcome some of these limitations to achieve microscale features such as holes and slots [4, 5] and deep hole drilling [6]. ECDM is primarily a thermal machining process occurring in an electrochemical cell. In ECDM, a direct current (DC) voltage is applied across electrodes that leads to the formation of hydrogen gas bubbles by electrolysis at the cathode. These bubbles grow and coalesce to form gas insulation of the tool eventually. When the gradual increase of the applied reaches a critical level, this gas film breaks down suddenly and causes high energy discharges. These discharges further heat up the electrolyte near the cathode forming vapors which further increase the thickness of the gas film as illustrated in Fig. 1. In an experimental study demonstrating the capability of machining complex structures in Pyrex glass by ECDM, it was reported that optimum combinations of both pulse voltage and tool rotational rate will realize better machining accuracy [4]. In another study, by reducing the concentration of the electrolyte used, deep hole drilling with an aspect ratio over 10 was achieved in glass by ECDM [6]. Yet, another experimental investigation revealed that thicker gas

Published online: 16 September 2019

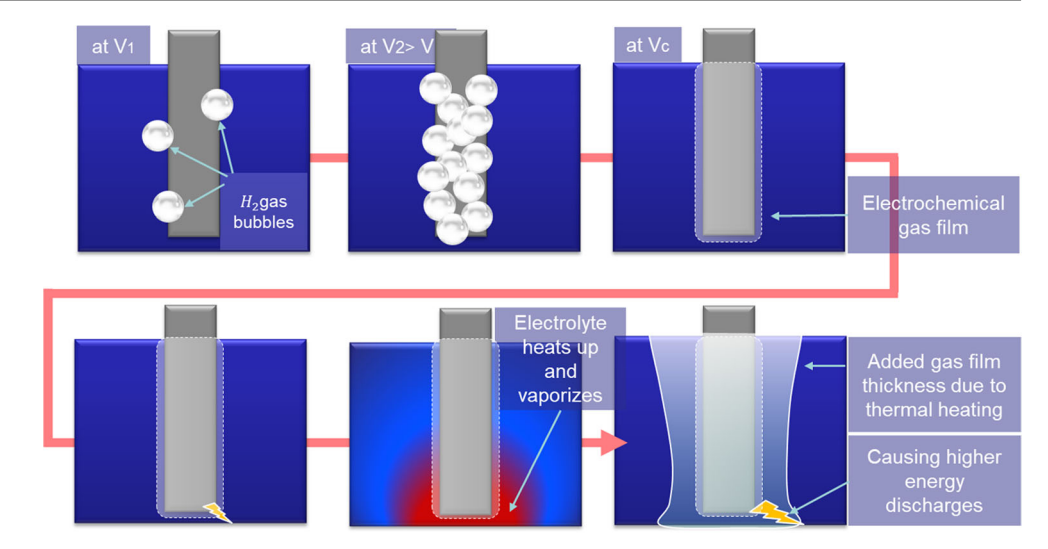


cracks, poor surface finish, low productivity, low aspect ratio machining, and in some cases, even safety hazards [3].

Murali Sundaram murali.sundaram@uc.edu

Department of Mechanical and Materials Engineering, University of Cincinnati, Cincinnati, OH 45221, USA

Fig. 1 Schematic of the gas film formation in the ECDM process (showing electrolyte near tool) where  $V_1$ ,  $V_2$ , and  $V_c$  are voltages applied to the electrochemical cell such that  $V_1 < V_2 < V_c$ , where  $V_c$  is the critical voltage at which gas film is formed



film causes higher energy discharges across the glass surface and affects the material removal in glass [7]. It was determined that in addition to the lower concentration of electrolyte, a lower level of electrolyte above the top surface of the workpiece also contributes to machining holes with minimal overcut and taper. As compared to ECDM with DC, the pulsed electrochemical discharge machining (PECDM) results in smaller hole diameter and smaller heat-affected zone (HAZ) [8]. The citations mentioned above obviously do not represent the extensive experimental studies performed in this field. However, they adequately demonstrate the potential of the ECDM process in glass machining. In addition to the experimental efforts, several attempts have been made to understand the ECDM process by simulation studies.

A review of previous research in the simulation of ECDM shows that material removal is simulated by different approaches. One of the approaches was to apply heat flux directly on the glass surface over a ring-shaped area that corresponds to the tool diameter to predict the material removal rate (MRR) [9]. Another study had approached the simulation by applying the plasma temperature on the glass surface over the area that corresponds to the plasma discharge diameter to predict the drilling depth and heat-affected zone [10]. In a yet another study, the heat of single discharge was applied in the form of Gaussian distribution [11]. From the material removal simulated by a single spark, the total MRR is predicted by considering the frequency of discharges [12]. An efficiency factor is often included in these calculations to account for the heat absorbed by the electrolyte near the cathode. However, in all these ECDM simulations, the heat flux has been applied directly on the surface of the glass without considering the electrolyte in the system, even though the experimental studies strongly suggest that the gas film influences the machining performance in ECDM [13]. For example, an experimental study of gas film in ECDM revealed the effect of surfactants in reducing the gas film thickness which resulted in improved accuracy of

Fig. 2 Schematic for the ECDM setup volume space modeled for simulation and the governing equations considering conservation of mass, momentum, and energy. (Phase change modeling in the equation is not shown because of space limitation). These boundary conditions and governing equations are explained in Table 1 and Section 2.2, respectively

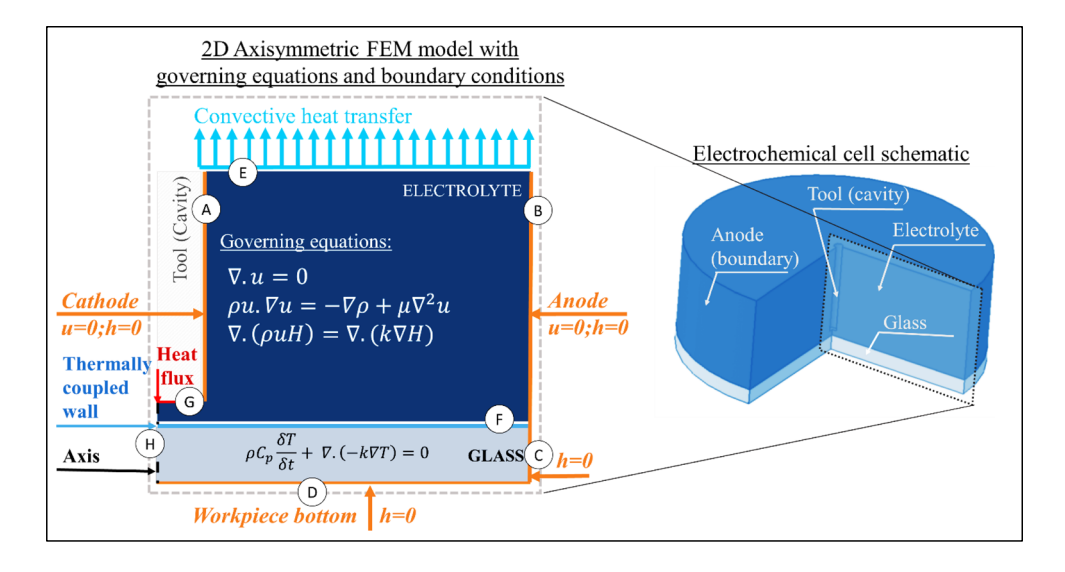
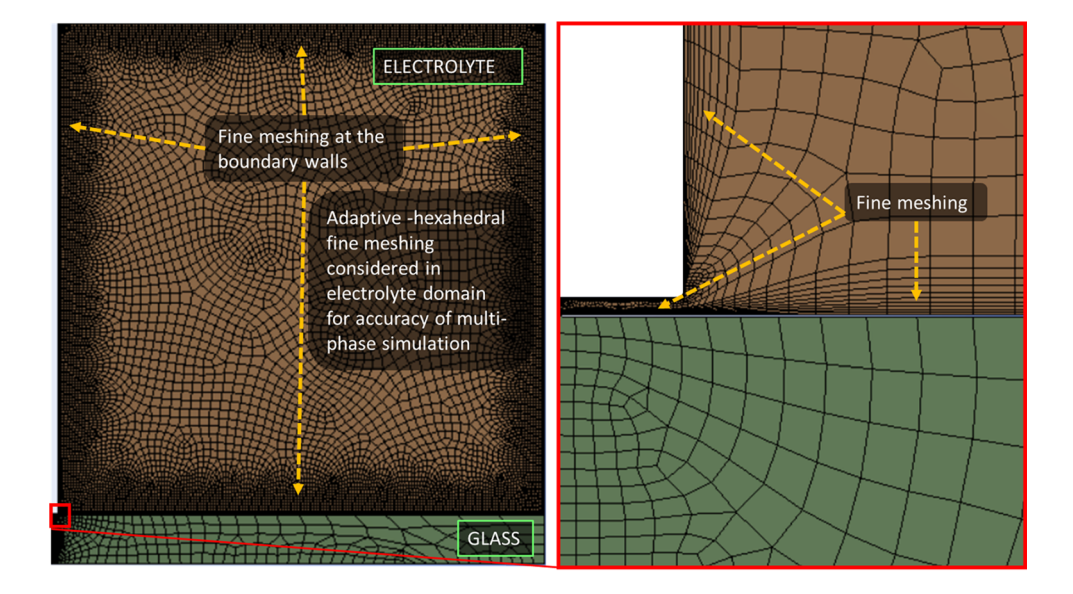




Fig. 3 Mesh applied to the system of electrolyte and glass with fine meshing at the boundaries



machining [14]. Another study focused on the tool properties by using side-insulated tool to achieve a thin gas film [15]. However, due to the stochastic nature of the ECDM process, it is very difficult to observe and analyze the role of gas film in ECDM by experimentation alone.

In this study, the finite element method is used for the simulation of the ECDM process to understand the impact of gas film characteristics on the overcut. The multiphase simulation setup incorporates a combined electrochemical system of glass and electrolyte. The changes in the gas film characteristics due to the variations in the level of and the corresponding changes in the overcut are studied as described in Section 2.

#### 2 Simulation studies

## 2.1 System description and boundary conditions

Simulation of ECDM was performed by 2-dimensional axisymmetric modeling of the electrolyte and the glass substrate below it. The system geometry and boundary conditions are shown in Fig. 2 and Table 1, respectively. The electrolyte is meshed, considering fine meshing layers at the wall boundaries as shown in Fig. 3 to capture the boundary layer accurately. The thickness of the fine mesh is less than the thickness of the theoretical boundary layer. Additionally, an adaptive mesh is applied near the surface of the tool where the phase change of electrolyte to vapor is expected. The material properties used in the simulation are given in Tables 2, 3, 4, and 5 [16]. The simulation conditions used are given in Table 6.

Properties of electrolyte and vapors used in the simulation are as presented in Tables 2, 3, 4, and 5.

#### 2.2 Governing equations

### 2.2.1 Fluid flow and heat transfer in electrolyte

The model for turbulent fluid conditions can be represented as given in Eq. (1) [17].

$$\frac{\delta}{\delta t}(\alpha_{\rm v}\rho_{\rm v}) + \nabla \cdot \left(\alpha_{\rm v}\rho_{\rm v}\overline{V}_{\rm v}\right) = \dot{m}_{\rm lv} - \dot{m}_{\rm vl} \tag{1}$$

**Table 1** Boundary conditions applied to the finite element system as shown in Fig. 2

	Boundary	Thermal boundary conditions, value
A	Cathode (tool) wall (excluding bottom)	Insulation and no flow, $u = 0$ ; $h = 0$
В	Anode (outer) wall	Insulation and no flow, $u = 0$ ; $h = 0$
C	Glass (outer) wall	Insulation, $h = 0$
D	Glass bottom	Insulation, $h = 0$
E	Electrolyte-air boundary	Convection and radiation, $h = 115$ ; $\epsilon = 0.95$
F	Glass-electrolyte boundary	Thermally coupled wall, wall thickness = $0$
G	Tool bottom surface	Heat flux = $(VI/\text{area of spark})$
H	Axis	Axis of revolution



 Table 2
 Temperature dependence of the density of the electrolyte

	Temperature									
	277	287	298	309.2	314.8	325.9	337	348.1	359.2	370.3
Density (kg/m <sup>3</sup> )	1000	999.75	998.02	995.1	993.18	988.7	983.38	977.29	970.56	963.33

 Table 3
 Temperature dependence of the heat capacity of the electrolyte

	Temperatu	Temperature								
	277	287	297	307	317	327	337	347	357	367
Heat capacity (J/kg/K)	4217.6	4181.8	4181.4	4178.4	4178.5	4180.6	4184.3	4189.5	4196.3	4205

Conservation equations of mass, momentum, and energy given in Eqs. (2–4) [17] were used to govern the fluid flow and heat transfer in the electrolyte.

Conservation of mass

$$\frac{\delta}{\delta t}(\rho_{\rm m}) + \nabla \cdot \left(\rho_{\rm m} \overline{\nu}_{\rm m}\right) = 0 \tag{2}$$

Conservation of momentum

$$\frac{\delta}{\delta t} \left( \rho_{\rm m} \overline{\nu}_{\rm m} \right) + \nabla \cdot \left( \rho_{\rm m} \overline{\nu}_{\rm m} \overline{\nu}_{\rm m} \right) = -\nabla p + \nabla \cdot \left( \mu_{\rm m} \left( \nabla \overline{\nu}_{\rm m} + \nabla \overline{\nu}_{\rm m}^T \right) \right) \quad (3)$$

Conservation of energy

$$\frac{\delta}{\delta t} \sum_{k=1}^{n} (\alpha_k \rho_k h_k) = \nabla . (k_{\text{eff}} \nabla T)$$
(4)

where v is the vapor phase,  $\propto_v$  is the vapor volume fraction,  $\rho_v$  is the vapor density,  $V_v$  is the vapor phase velocity, and  $\dot{m}_{1v}$  and  $\dot{m}_{v1}$  are the rates of mass transfer due to evaporation and condensation, respectively.  $\propto_k$  is the volume fraction of phase k,  $\rho_m$  that is equal to  $\sum_i \propto_i . \rho_i$  is the density of multiphase fluid phases,  $\overline{v}_m$  that is equal to  $\frac{\sum_i \propto_i . \rho_i . v_i}{\rho_m}$  is the velocity of multiphase fluid (mass averaged velocity),  $h_k$  is the standard state enthalpy of phase k,  $k_{\rm eff}$  that is equal to  $\sum_i \propto_i . k_i$  is the effective conductivity of multiphase fluid,  $\mu_m$  that is equal to  $\sum_i \propto_i . \mu_i$  is the viscosity of multiphase fluid phases, and T is the temperature of the multiphase fluid.

The Wilcox k- $\omega$  turbulence model, shown in Eq. (1), also considers the effect of viscosity and shear stress at very high temperatures near the wall region. The variations in density, viscosity, and heat capacity of the fluid with respect to the temperature are considered as shown in Tables 2, 3, and 4. This aids in simulating the changes in buoyancy and the natural convective flow.

A two-phase fluid system (liquid and gas) is simulated to incorporate the evaporation of the electrolyte during the process as outlined in Fig. 4. In such a multiphase system, each mesh element has access to the properties of both the liquid electrolyte and the vapors. These properties are triggered by the standard state enthalpy of the element. The difference in the values of the standard state enthalpy of the vapor phase and that of the liquid phase is equal to the latent heat of evaporation. When the standard state enthalpy of the vapor is reached within a mesh element, the electrolyte in that particular mesh element changes phase from a liquid electrolyte to vapor. In this way, the multiphase simulation setup helps simulate the gas film formation.

The heat flux in ECDM which affects the gas film formation and the overcut is the cumulative result of the random discharges happening in the system. The random distribution of sparks, their energy, and their frequency are input into the system using a user-defined function (UDF). Heat flux is applied periodically for a number of time steps corresponding to the mean discharge frequency. The discharge location is picked randomly by UDF, and the heat flux is given over the circular area corresponding to the discharge radius. The heat

 Table 4
 Temperature dependence of the viscosity of the electrolyte

	Temperature									
	277	287	297	307	317	327	337	347	357	367
Viscosity (kg/m/s × 10 <sup>-6</sup> )	1792.1	1307.7	1005	800.7	656	549.4	468.8	406.1	363.5	316.5



Table 5 Material properties of electrolyte, vapor, and glass

Parameter	Value
Thermal conductivity of water (W/m/K)	0.6
Standard state enthalpy of water (J/kg/mol)	0
Thermal conductivity of vapor (W/m/K)	0.02
Density of vapor (kg/m <sup>3</sup> )	0.5542
Specific heat of vapor (J/kg/K)	2014
Viscosity of vapor (kg/m/s)	$1.34 \times 10^{-6}$
Standard state enthalpy of water (J/kg/mol)	40.8
Convective heat transfer at the air boundary (W/m²/K)	115
Density of glass (kg/m <sup>3</sup> )	2230
Specific heat of glass (J/kg/K)	830
Thermal conductivity of glass (W/m/K)	1.14

flux can be calculated as shown in Eq. (5), where the radius of discharge ( $R_{\rm discharge}$ ) is given by Ikai and Hashiguchi [18] model as shown in Eq. (6)

Heat flux (W·m<sup>2</sup>) = 
$$\frac{V_{\text{critical}} \times I_{\text{discharge}}}{\pi R_{\text{discharge}}^2}$$
(5)

$$R_{\rm discharge} = 2040 \times I^{0.43} \times t_{\rm discharge \ on \ time}^{0.44}$$
 (6)

where  $V_{\rm critical}$  is the critical voltage (V),  $I_{\rm discharge}$  is the mean discharge current (A),  $t_{\rm discharge}$  on time (s), and  $R_{\rm discharge}$  is the radius of discharge (m).

These values of discharge current and discharge time interval are recorded in the experimentation via current probe and oscilloscope. An example of these recordings is shown in Fig. 5.

Heat transfer in glass due to heat flux is computed with Eq. (7) [19]

$$\rho C_{\rm p} \frac{\delta T}{\delta t} + \nabla \cdot (-k \nabla T) = Q \tag{7}$$

Table 6 Simulation conditions

2D axisymmetric thermal transient Analysis type Elements used Quadrilateral; hexahedral adaptive mesh Pressure velocity coupling algorithm Pressure implicit with splitting operator (PISO) Time step Meshing type Mapped mesh with fine mesh at the walls Convective heat transfer coefficient at air 115 boundary (W/m<sup>2</sup>/K) 0.95 Radiation coefficient Workpiece material Borosilicate glass Thickness of the workpiece  $(H \times L)$  $1 \text{ mm} \times 10 \text{ mm}$ Electrolyte domain size  $(H \times L)$ 3 mm  $\times$  10 mm; 5 mm  $\times$  10 mm; 10 mm  $\times$  10 mm for 3 variations Total time of simulation 2 s

where  $\rho$  is the density,  $C_p$  is the specific heat capacity, k is the heat conductivity, and T is the absolute temperature (K).

#### 2.3 Assumptions

The assumptions made during the simulation are given below:

- The material removal by other possibilities such as chemical reactions and mechanical weathering is deemed negligible and neglected.
- An ideal situation of smooth tool surface and the presence of initial layer of gas film formed by electrolysis are assumed.
- 3. The change in surface tension of electrolyte due to the change in temperature is neglected.
- 4. Increase in vapor pressure at the top air boundary due to vaporization is neglected.

#### 3 Simulation results and discussion

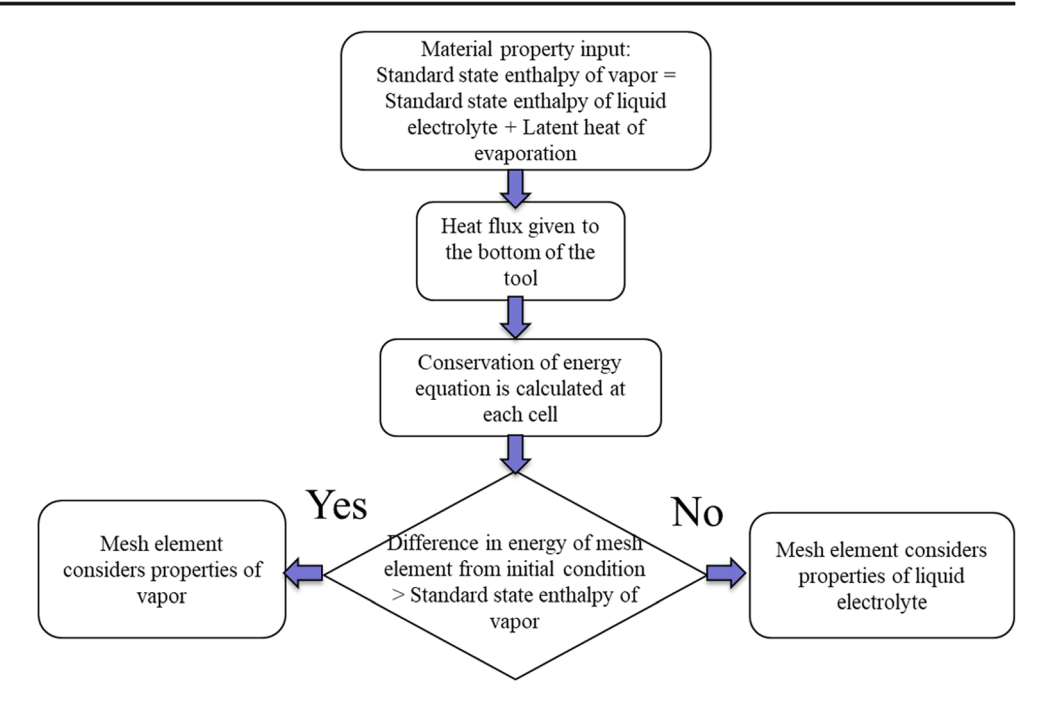
The results are discussed in two subsections. In Section 3.1, the gas film characteristics are studied along with the overcut in machining for variation in the level of electrolyte. Section 3.2 discusses the experimental validation for the findings of the gas film characteristics and corresponding overcut in machining.

# 3.1 Effect of level of electrolyte on the gas film formation

Varying levels of electrolyte showed a significant effect on the gas film thickness, its shape, and stability. When the level of the electrolyte was increased in the simulation, it resulted in an



**Fig. 4** Multiphase simulation methodology



increase in the thickness of the gas film with a wider spreading shape at the glass interface, as shown in Fig. 6.

In Fig. 6, the vapor fraction is plotted at the glass interface in the radial direction for different levels of electrolyte. The region where the vapor fraction is 1 is considered as the gas film, and the thickness is calculated accordingly. The contour plots of vapor fraction are also shown in Fig. 6 where red color represents the gas film. The spreading shape of the gas film near the tool bottom and its effect on the gas film thickness at the glass interface can be observed in these contour plots. This shape is also an important factor because it indicates the spatial range of the discharges which affect the glass, and thus affects the overcut in the machining.

This change in the shape of the gas film with variation in the level of the electrolyte can be explained by studying the

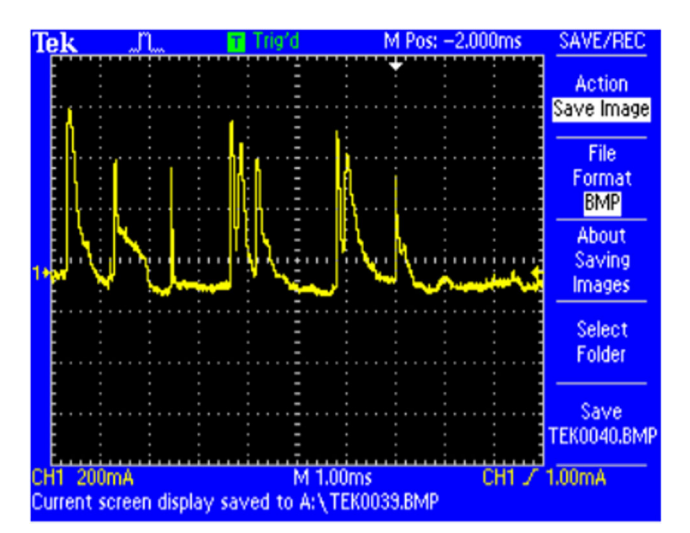


Fig. 5 Current probe recording of discharge current activity

hydrodynamic behavior in the electrolytic cell. While studying the hydrodynamic behavior, buoyancy-driven convective flow formation was observed for all the variations. Formation of such a convective flow is shown in Fig. 7.

Figure 7 shows the gas film formation using vapor-phase contours for a 10 mm depth of electrolyte along with the normalized vector plots of velocity at the time shown by numbers in each window. The vector plot shows the onset of the circular convective flow field, which carries vapors of the electrolyte along with the flow. Studying the convective vector plot along with the respective vapor contours a–c, for every

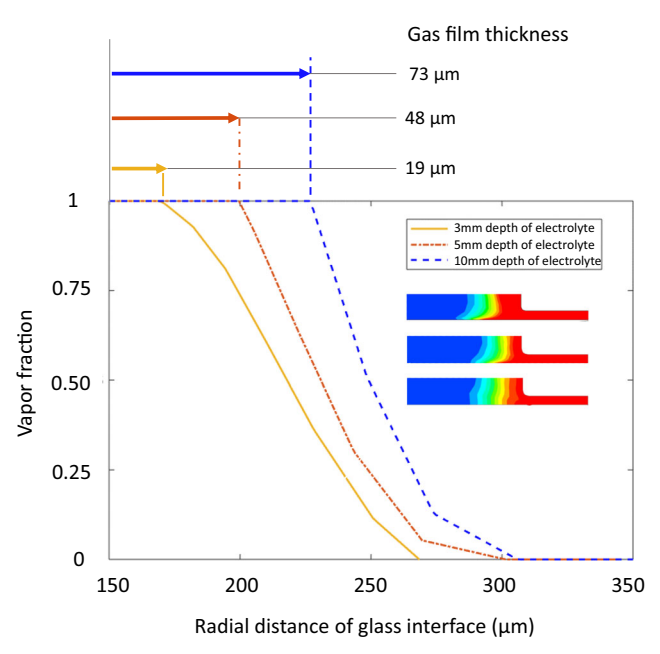


Fig. 6 Gas film thickness for the variation of the level of electrolyte



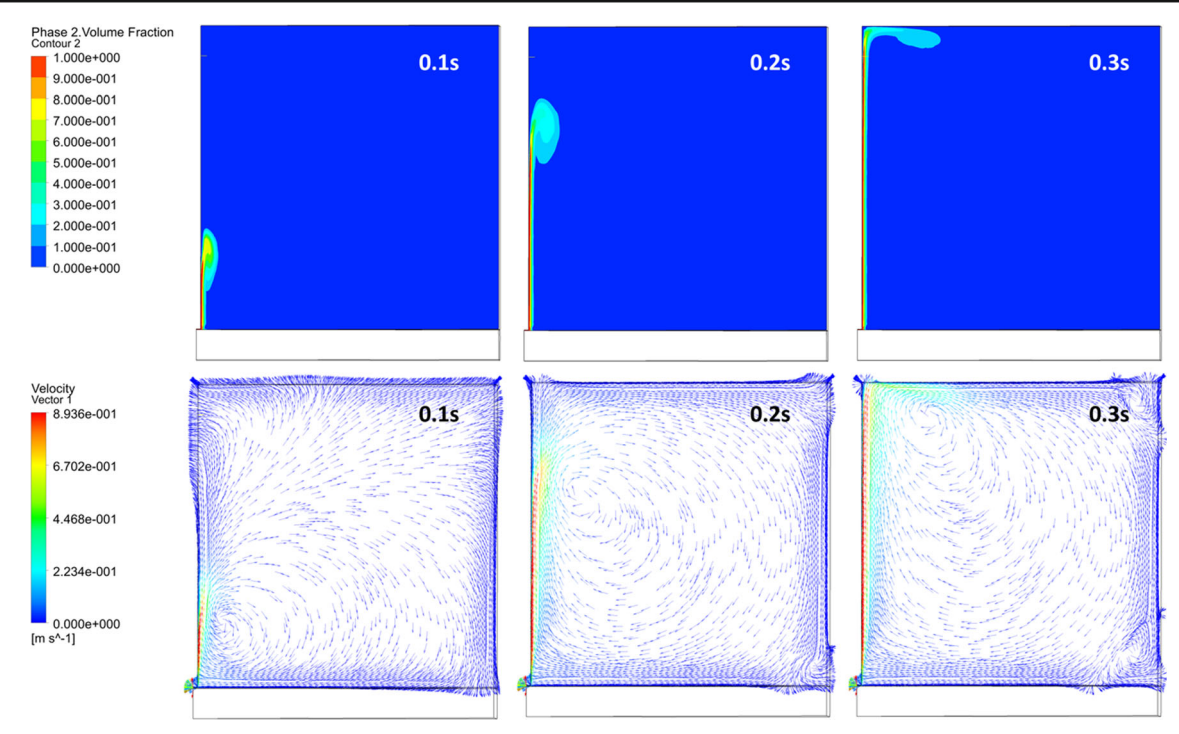


Fig. 7 Gas film formation for a 10 mm depth of electrolyte for 0.1 s, 0.2 s, and 0.3 s. Top, contours of vapors. Bottom, vector plots of the flow within the electrolytic cell

time step, shows that the height of the gas film is right above the center of the circular flow field. Therefore, the shape of the convective flow field is deemed as a controlling factor which affects the shape and the thickness of the vapor gas film.

The literature on thermal convective flow reports that the shape of the flow pattern depends on the intensity of the convective flow [20]. This intensity can be studied using the non-dimensional Nusselt number, which is the ratio of convective heat transfer to conductive heat transfer in the system. The Nusselt number in Fig. 8 shows an increase with an increase in the level of electrolyte. This explains that as the level of electrolyte increases, the convective heat transfer becomes more dominant. As a result, a unique shape of convective flow

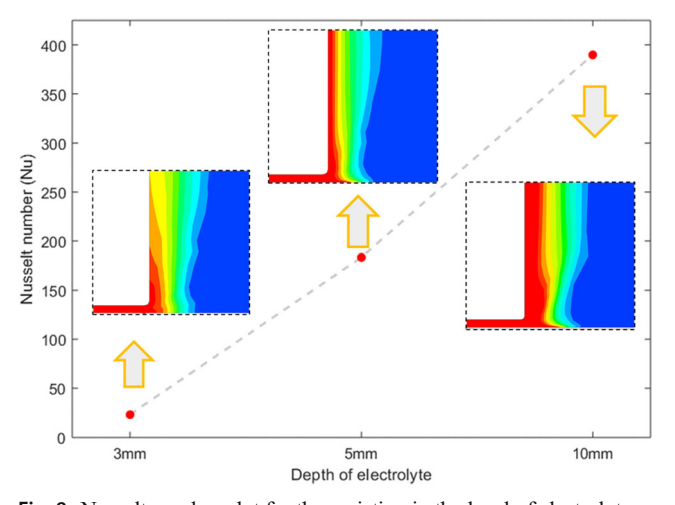


Fig. 8 Nusselt number plot for the variation in the level of electrolyte

is observed for each variation. Figure 9 shows the velocity vector plot for each level of electrolyte. It can be observed that as the intensity of the convective flow increased, the radius of the flow field also increased. This unique shape of the convective flow field for each variation defines the gas film spread at the bottom. Therefore, the spread of the gas film increased for an increasing level of electrolyte as shown in Fig. 8.

Another aspect which can affect the overcut in machining is the stability of the gas film shape. The literature study yields that the Reynolds number value greater than 2000 produces instability in shear flows [21]. The percentage of the number of nodes on the gas film boundary with a value higher than 2000 is considered as the predicting factor for the stability of the gas film. An increase in the level of electrolyte also showed an increase in the percentage of nodes with the Reynolds number value higher than 2000 (Fig. 10), which indicates an increase in the instability of the gas film shape. Therefore, it is clear that the gas film becomes thicker and more unstable as the level of electrolyte increased.

# 3.2 Effect of the level of electrolyte on the overcut in machining

Figure 11 shows contours of gas film and the glass melts for different levels of electrolyte at the end of 2 s of machining. The overcut in machining is calculated as the difference between the radial crater radius and the radius of the tool. It can be seen that a higher level of electrolyte produced a thicker gas



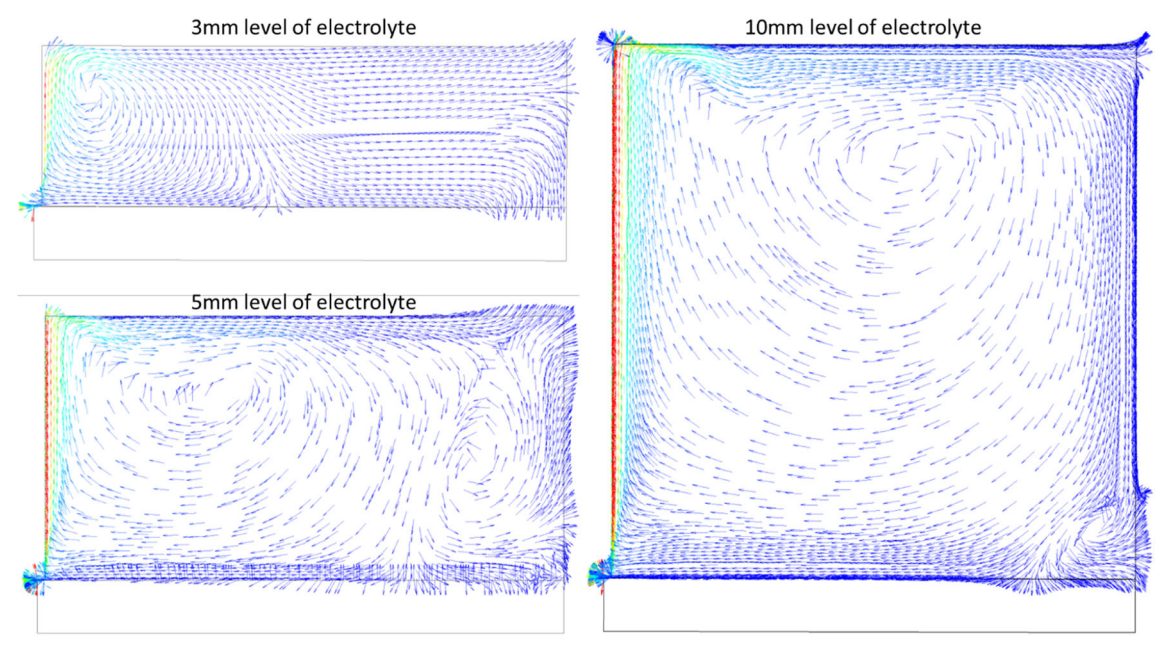


Fig. 9 Vector plot of velocity of electrolyte with variation in the level of electrolyte

film, which, as a result, produced more radial overcut in the workpiece. Additionally, it can be observed that the depth of cut is higher for lower gas film thickness, which is more suitable for through-hole machining with low taper. Section 4 details the experimental validation performed for the findings in this simulation study.

## 4 Experimental validation

ECDM experiments were carried out using an in-house-built experimental system shown in Fig. 12.

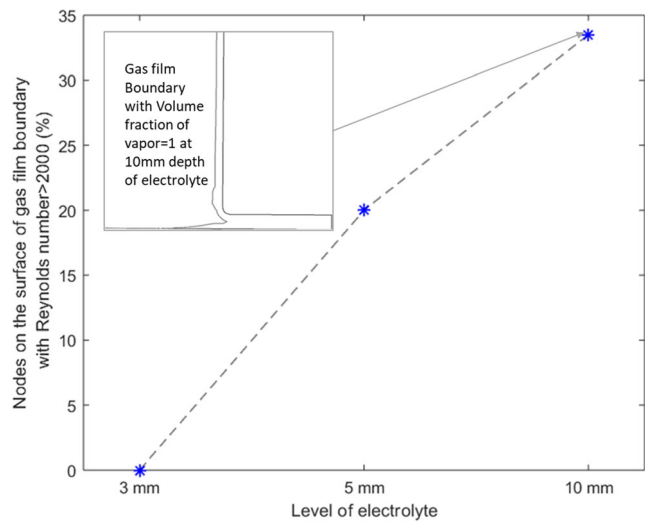


Fig. 10 Average Reynolds number at the gas film boundary for variation in the level of electrolyte



A hollow ring (5-mm-thick tool steel block with an internal diameter of 20 mm) and a tungsten rod (diameter 300  $\mu$ m) were used as anode and cathode, respectively. Sodium hydroxide (NaOH) electrolyte was used with 1 M concentration. The ECDM machining experiments were performed for 2 s on 200- $\mu$ m-thick borosilicate glass using different experimental conditions listed in Table 7. A current probe (Tektronix TCP2020) is used to record discharge on-off times and discharge current after the onset of sparks. The critical voltage for each experimentation is recorded. The energy of discharge is calculated as given in Eq. (9). Each experiment was repeated five times to mitigate the experimental uncertainties. Table 7 shows the respective critical voltage, the average current value, and the spark on time for respective electrolyte concentration.

#### 4.1 Optical verification of gas film thickness

Figure 13 shows the trend of gas film thickness from experimental observations with respect to the variation in the level of electrolyte. The increase in gas film thickness with an increase in the level of electrolyte observed in these experimental results validates similar trends revealed by simulation (Fig. 6).

#### 4.2 Verification of overcut predictions

Profiles of the craters formed in the experimentation were plotted using a profilometer. These experimental crater profiles and the simulated crater contours were compared by superimposing them as shown in Fig. 14.

In Fig. 14, the red thick profile shows a simulated crater shape and the blue dotted line shows the experimental profile of the machining. For all the experimental runs, the simulation

**Fig. 11** Comparison of the gas film thickness and the glass melt contours

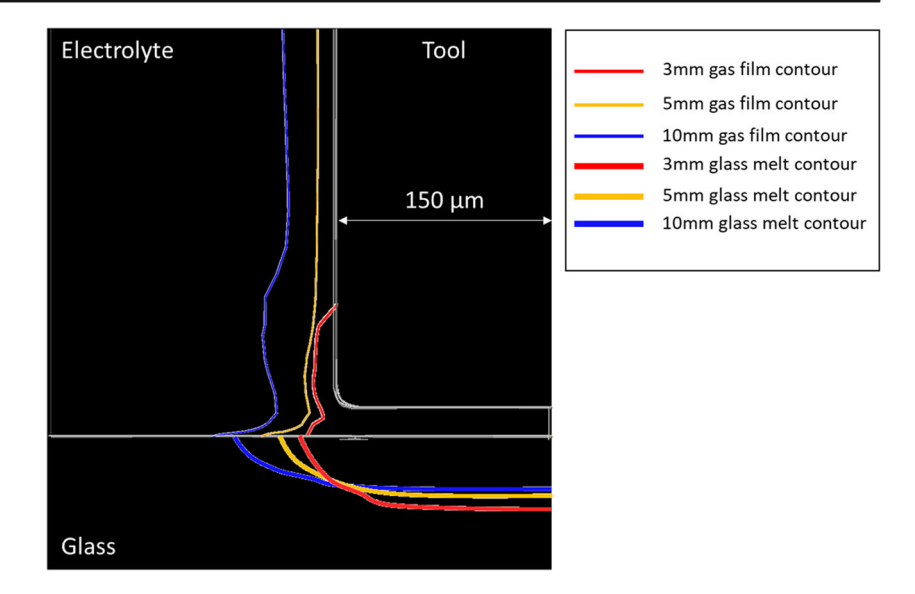
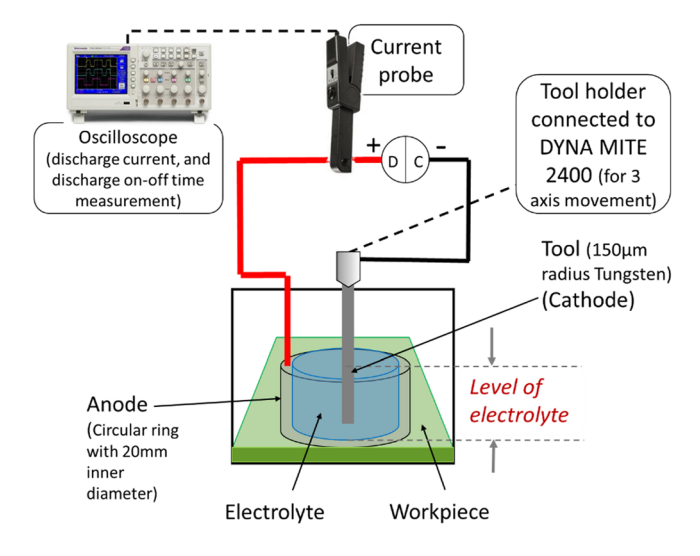


Fig. 12 Schematic of the experimental setup (left) and illustration of the different levels of electrolyte (right)



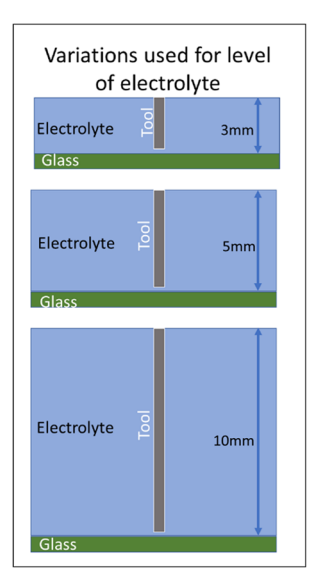


 Table 7
 Experimental parameters

Experimental parameters	Values
Electrolyte	Sodium hydroxide
Cathode	Tungsten microtool (150 µm) radius
Anode	Hollow stainless steel ring of 20 mm diameter and 20 mm height
Time of machining	2 s
Concentration of electrolyte	1 M
Levels of electrolyte	(a) 3 mm, (b) 5 mm, (c) 10 mm from the glass surface
Average critical voltage	(a) 39.4 V, (b) 40.7 V, (c) 43.1 V
Workpiece	Borosilicate glass (1 mm thickness)



**Fig. 13** Optical validation of the increasing trend of gas film thickness with an increase in the level of electrolyte



and experimental contours were compared to check the radial overcut and depth of cut of machining. The radial overcut in the machining is calculated as the difference between the radius of the machined crater and the radius of the tool. Figure 15 shows the radial overcut values for the various levels of

electrolyte for simulated and experimented craters. The trend of increase in overcut with an increase in the level of electrolyte was observed in both simulation and experimental results. The variations in the overcut predictions made by the simulations are within 12% to 23% of the experimental results.

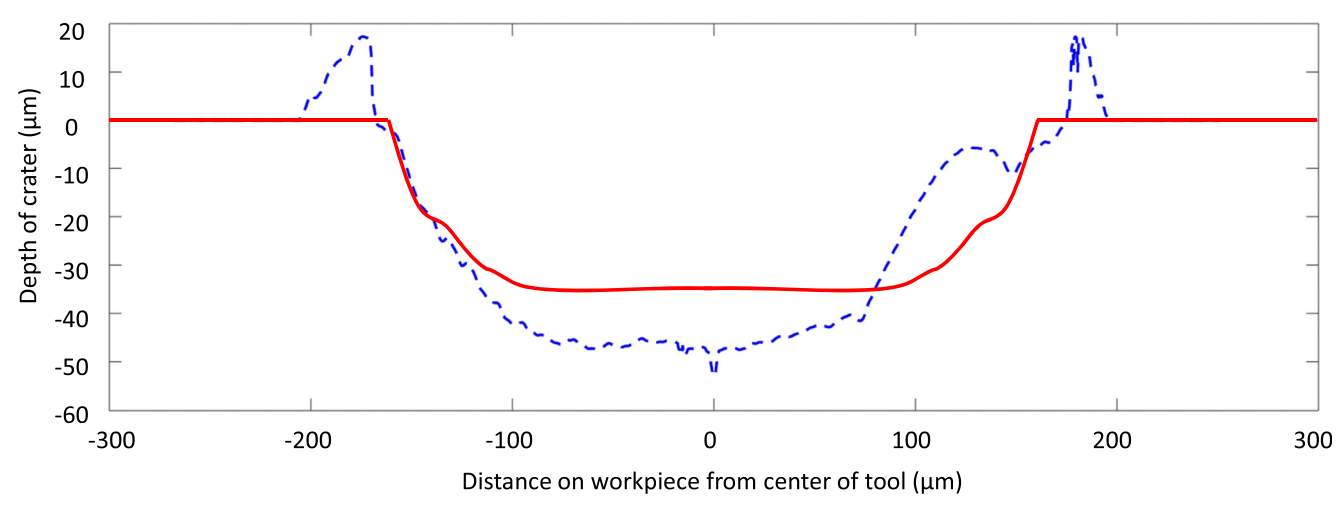


Fig. 14 Comparison of the simulated and experimented craters



**Fig. 15** Comparison of the simulated and experimented overcut in the machining

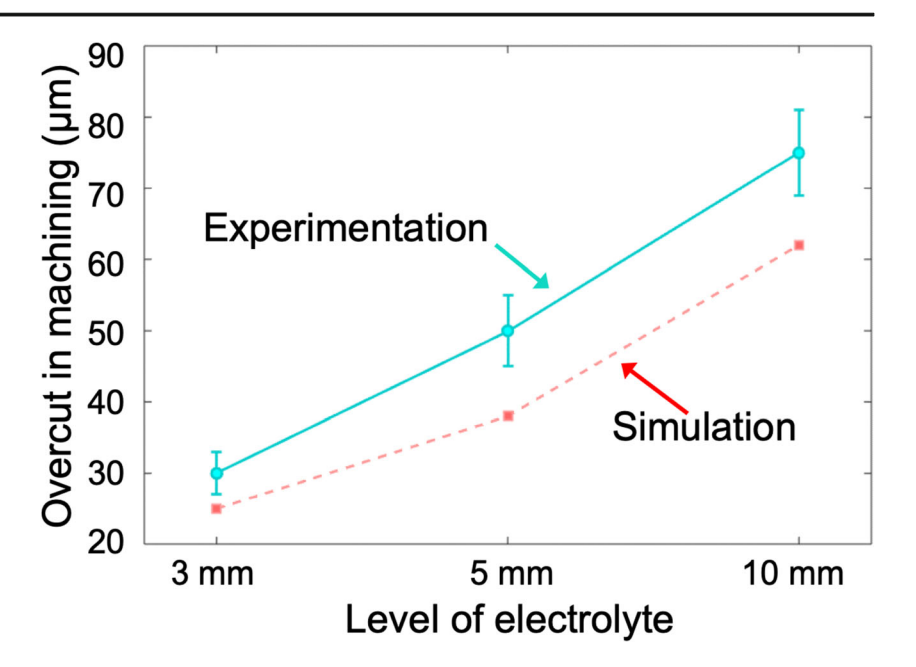


Figure 16 shows cross sections of through holes machined for each level of electrolyte. It was observed that the entry diameters are larger for a higher level of electrolyte due to the wider spreading shape of the gas film. Also, more tapered holes were observed for a higher level of electrolyte.

As evident from the simulation results of Fig. 11, the depth of cut is more for the lower level of electrolyte with less entry diameter. This finding is supported by the cross sections of the through hole from Fig. 16, and it verifies that the lower level of electrolyte is more suitable for through hole machining.

#### **5 Conclusion**

A first attempt using a multiphase finite element simulation was performed to understand the impact of gas film

characteristics on the overcut in the electrochemical discharge machining process. The multiphase simulation setup incorporates a combined electrochemical system of glass and electrolyte. The changes in the gas film characteristics due to the variations in the level of and the corresponding changes in the overcut are studied. Simulations revealed that as the level of electrolyte increases, the convective heat transfer becomes more dominant and the shape of the convective flow field affects the shape and the thickness of the gas film. The simulated depth of cut was found to be higher for lower gas film thickness, which is more suitable for through-hole machining with low taper. It was observed that the gas film thickness increased with an increase in the level of electrolyte and the gas film stability showed an opposite trend. This resulted in an increase in the overcut in the machining with the increase in the level of electrolyte. This trend observed in the simulation was validated with experimentation.

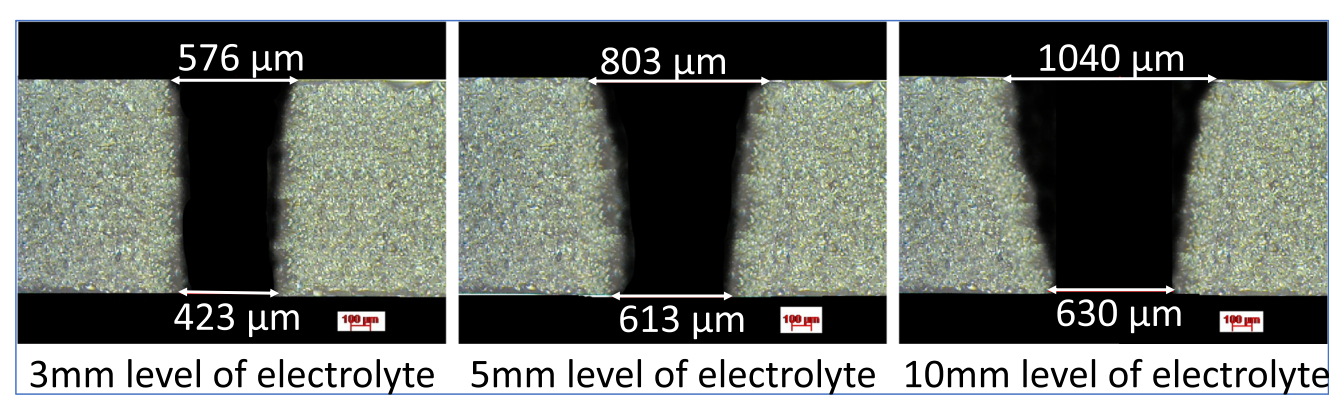


Fig. 16 Cross sections of through hole machining for the 3 mm, 5 mm, and 10 mm levels of electrolyte



Acknowledgments This material is based upon the work supported by the National Science Foundation (Grant No. CMMI-1833112). Any opinions, findings, and conclusions or recommendations expressed in this material are those of the author(s) and do not necessarily reflect the views of the National Science Foundation.

#### References

- Liang Y, Dutta SP (2001) Application trend in advanced ceramic technologies. Technovation 21(1):61–65. https://doi.org/10.1016/ S0166-4972(00)00019-5
- Stjernström M, Roeraade J (1998) Method for fabrication of microfluidic systems in glass. J Micromech Microeng 8(1):33–38
- Takeuchi Y, Sawada K, Sata T (1996) Ultraprecision 3D micromachining of glass. CIRP Ann Manuf Technol 45(1):401– 404. https://doi.org/10.1016/S0007-8506(07)63090-X
- Zheng Z-P, Cheng W-H, Huang F-Y, Yan B-H (2007) 3D microstructuring of Pyrex glass using the electrochemical discharge machining process. J Micromech Microeng 17(5):960–966
- Yang CT, Song SL, Yan BH, Huang FY (2006) Improving machining performance of wire electrochemical discharge machining by adding SiC abrasive to electrolyte. Int J Mach Tools Manuf 46(15): 2044–2050. https://doi.org/10.1016/j.ijmachtools.2006.01.006
- Jui SK, Kamaraj AB, Sundaram MM (2013) High aspect ratio micromachining of glass by electrochemical discharge machining (ECDM). J Manuf Process 15(4):460–466. https://doi.org/10.1016/ i.imapro.2013.05.006
- Kolhekar KR, Sundaram M (2018) Study of gas film characterization and its effect in electrochemical discharge machining. Precis Eng 53:203–211. https://doi.org/10.1016/j.precisioneng.2018.04.002
- Sundaram M, Chen Y-J, Rajurkar K (2019) Pulse electrochemical discharge machining of glass-fiber epoxy reinforced composite. CIRP Ann 68:169–172. https://doi.org/10.1016/j.cirp.2019.04.113
- Abou Ziki JD, Hof LA, Wüthrich R (2015) The machining temperature during spark-assisted chemical engraving of glass. Manuf Lett 3:9–13. https://doi.org/10.1016/j.mfglet.2014.11.003
- Krötz H, Roth R, Wegener K (2013) Experimental investigation and simulation of heat flux into metallic surfaces due to single discharges in micro-electrochemical arc machining (micro-

- ECAM). Int J Adv Manuf Technol 68(5):1267–1275. https://doi.org/10.1007/s00170-013-4918-9
- Jiang B, Lan S, Ni J, Zhang Z (2014) Experimental investigation of spark generation in electrochemical discharge machining of nonconducting materials. J Mater Process Technol 214(4):892–898. https://doi.org/10.1016/j.jmatprotec.2013.12.005
- Goud M, Sharma AK (2017) A three-dimensional finite element simulation approach to analyze material removal in electrochemical discharge machining. Proc Inst Mech Eng C J Mech Eng Sci 231(13):2417–2428
- Fascio V, Langen HH, Bleuler H, Comninellis C (2003) Investigations of the spark assisted chemical engraving. Electrochem Commun 5(3):203–207. https://doi.org/10.1016/ S1388-2481(03)00018-3
- Wüthrich R, Hof LA, Lal A, Fujisaki K, Bleuler H, Ph M, Picard G (2005) Physical principles and miniaturization of spark assisted chemical engraving (SACE). J Micromech Microeng 15(10): S268–S275
- Min-Seop H, Byung-Kwon M, Sang Jo L (2008) Modeling gas film formation in electrochemical discharge machining processes using a side-insulated electrode. J Micromech Microeng 18(4):045019
- Haynes WM (2014) CRC handbook of chemistry and physics. CRC
- Hassanizadeh M, Gray WG (1979) General conservation equations for multi-phase systems: 2. Mass, momenta, energy, and entropy equations. Adv Water Resour 2(4):191–203
- Ikai T, Hashiguchi K (1995) Heat input for crater formation in EDM. In: Proceedings of the International Symposium for Electro-Machining-ISEM XI, EPFL. pp. 163–170
- Frank PI, David PD (1981) Fundamentals of heat transfer. Wiley, New York
- Bhuvaneswari M, Sivasankaran S, Kim YJ (2011) Effect of aspect ratio on convection in a porous enclosure with partially active thermal walls. Comput Math Appl 62(10):3844–3856. https://doi.org/ 10.1016/j.camwa.2011.09.033
- Avila K, Moxey D, de Lozar A, Avila M, Barkley D, Hof B (2011)
   The onset of turbulence in pipe flow. Science 333(6039):192–196

**Publisher's note** Springer Nature remains neutral with regard to jurisdictional claims in published maps and institutional affiliations.

